JOURNAL OF GUIDANCE, CONTROL, AND DYNAMICS
Vol. 31, No. 3, May–June 2008

Experimental and Theoretical Development of Multiple Fluid Mode Magnetorheological Isolators

Mikel Brigley,* Young-Tai Choi,† and Norman M. Wereley‡
University of Maryland, College Park, Maryland 20742

DOI: 10.2514/1.32969

The experimental and theoretical development of a multiple fluid mode magnetorheological isolator is addressed in this study. First of all, a multiple fluid mode magnetorheological isolator that operates using shear, flow, and squeeze modes, and can isolate multi-degree-of-freedom excitations, is configured and fabricated. The damper characteristics of the magnetorheological isolator are experimentally evaluated using metrics of equivalent viscous damping and complex stiffness. To analytically predict the damper characteristics of the magnetorheological isolator, the Bingham-plastic isolator model is constructed and its important model parameters are identified using an averaging method derived from sinusoidal force-displacement and force-velocity data. Comparison of the measured and predicted results using the Bingham-plastic isolator model is conducted. To improve model prediction ability, a nonlinear hysteretic model is introduced. Comparison of the two isolator models is conducted using extensive experimental results.

Introduction

IN RECENT years, vibration attenuation in aerial vehicles has attracted increasing attention because sensitive instruments and payloads, exposed to severe and unwanted vibration, have experienced malfunctioning components, shorter lifetime, and degradation of overall operational performance [1,2]. A promising solution to achieve vibration attenuation is to place vibration isolators using magnetorheological (MR) fluids into the vibration transmission path to isolate precision payloads from disturbance sources.

For the development of MR isolators, three working fluid modes of damper operation are available: shear mode [3–7], flow mode [8–13], and squeeze mode [14–18]. When one of two magnetic poles moves linearly or rotationally relative to the other, the shear mode occurs. In the shear mode, the fluid is directly sheared by relative motion of these surfaces. The flow mode is developed when pressurized flow passes through a rectangular or annular duct formed by two magnetic poles. Use of each fluid mode gives merits and demerits to the design of MR isolators. Flow-mode isolators can produce higher damper force at compact size, but have a detrimental lockup state in which the flow in the MR valve does not occur. Shear-mode isolators do not undergo the lockup state, but produce smaller damper force. Squeeze-mode isolators also do not have the lockup state, but their damper force shows strongly nonlinear behavior at excitation displacement and are effective at small vibration. Therefore, in this study, an MR isolator using multiple fluid modes is developed so as to maximize the damping capability, and experimental and theoretical analyses are conducted. To realize this goal, a multiple fluid mode MR isolator that operates using shear, flow, and squeeze modes, and can isolate multi-degree-of-freedom excitations, is configured and fabricated. The damper characteristics of the MR isolator are experimentally evaluated using metrics of equivalent viscous damping and complex stiffness. To analytically predict the damper characteristics of the MR isolator, the Bingham-plastic isolator model is constructed and its important model parameters are identified using an averaging method derived from sinusoidal force-displacement and force-velocity data. Comparison of the measured and predicted results using the Bingham-plastic isolator model is conducted. To improve the model prediction ability, the nonlinear hysteretic model is used. Comparison of the two isolator models over several damper performance plots, such as the force-displacement, force velocity, equivalent viscous damping, and complex stiffness, is conducted using the experimental results.

Received 21 June 2007; revision received 31 October 2007; accepted for publication 2 November 2007.

*Graduate Research Assistant, Smart Structures Laboratory, Department of Aerospace Engineering.

†Assistant Research Scientist, Smart Structures Laboratory, Department of Aerospace Engineering.

‡Professor, Smart Structures Laboratory, Department of Aerospace Engineering, Corresponding Author. Associate Fellow AIAA.

Design and Fabrication

The multiple fluid mode MR isolator designed and fabricated in this study is presented in Fig. 1. The electromagnetic coil is wrapped around the bobbin and the outer cylinder works as a magnetic flux return. The bobbin is attached to the top elastomer through the connecting screw. As a result, the motion of the elastomer results in the motion of the bobbin and the bobbin motion produces radial flow of the fluid in the gap between the bottom of the bobbin and the outer cylinder. This radial flow causes the MR isolator to have squeeze-mode damping. At the same time, bobbin motion also induces flow passing back and forth between chambers at its top and bottom. From this flow, shear- and flow-mode damping occurs at the MR isolator. The height and the outer diameter of the MR isolator are 69 and 52 mm, respectively. The bobbin and the outer cylinder were made from 1018 carbon steel and 24 gauge copper wire was wound around the bobbin. There were 188 turns of the wire upon completion of winding. Note that, in single-flow mode MR isolators, when a high-yield stress or a small amplitude excitation input is applied, the lockup state may occur. In the lockup state, single-flow mode MR isolators produce no damping and work as passive stiffeners. However, in the multiple fluid mode MR damper, the elastomer is connected to the bobbin, so that the lockup state cannot occur.

Figure 2 presents the finite element analysis (FEA) of the magnetic density in the gap of the MR isolator. As seen in this figure, the gaps at the bottom and the top of the bobbin, excluding the coil area, are magnetically active. This allows all of the operating modes (shear, squeeze, and flow) to exploit the MR effect when a current input is applied.

Experimental Analysis

The damper characteristics of the multiple fluid mode MR isolator is experimentally evaluated using an MTS Systems Corporation machine as shown in Fig. 3. In this case, the excitation frequency is varied from 5–20 Hz in increments of 1 Hz, with additional cases of

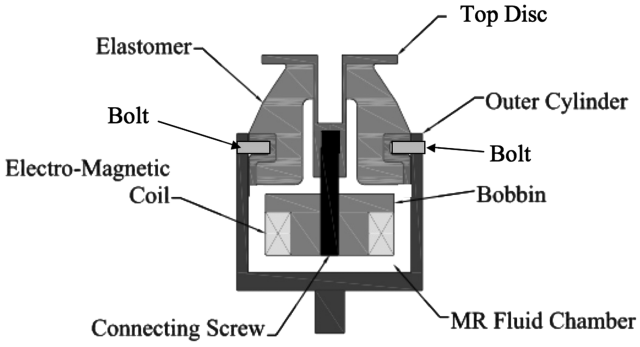

a) Schematic diagram

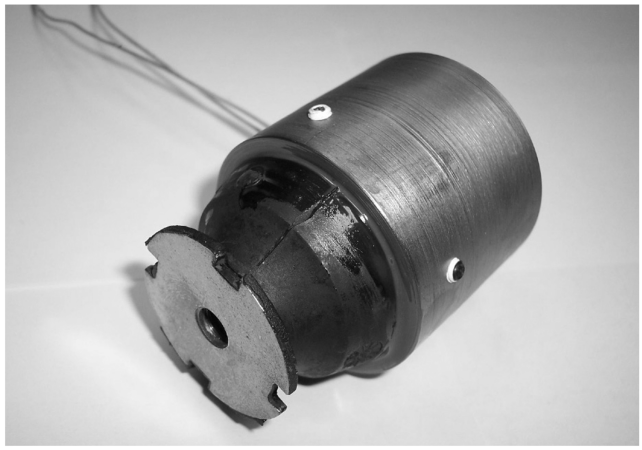

b) Fabricated isolator

Fig. 1 Multiple fluid mode MR isolator using the shear, flow, and squeeze mode.

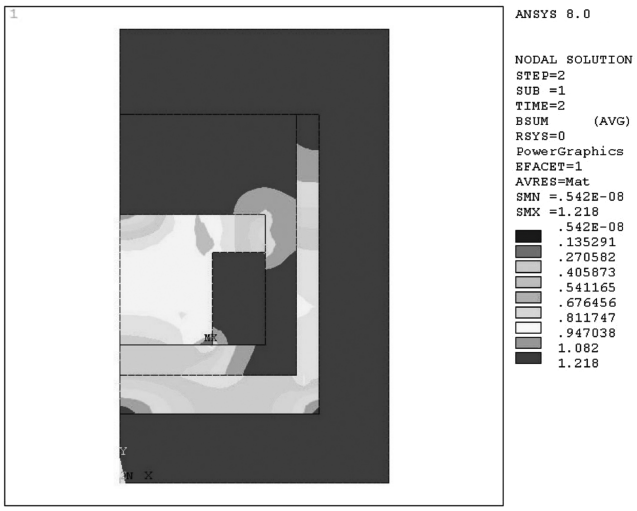

Fig. 2 Finite element analysis of the magnetic density in the gap of the MR isolator.

1 Hz and 2.5 Hz excitation. The displacement amplitudes consist of 0.1, 0.25, 0.5, and 0.75 mm. The applied current ranges from 0–2 A in increments of 0.5 A. Hybrid MR fluid that has 80% loading by weight of solid particles and 90% microsized particles and 10% nanosized particles is used.

To analyze the damper characteristics of the multiple fluid mode MR isolator, a standard linearization technique, equivalent damping, is used in this study. The equivalent viscous damping is computed by equating the energy dissipated by the MR isolator over a single cycle E at a given frequency ω to that of the viscous damping. The energy dissipated by the MR isolator is calculated [19,20] using

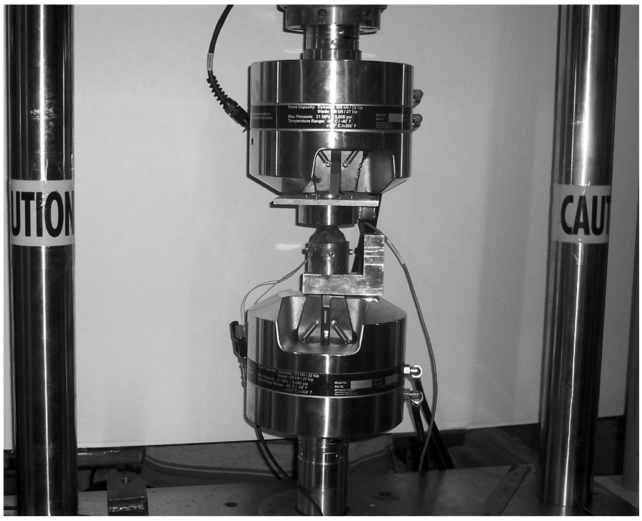

Fig. 3 Experimental testing of the MR isolator.

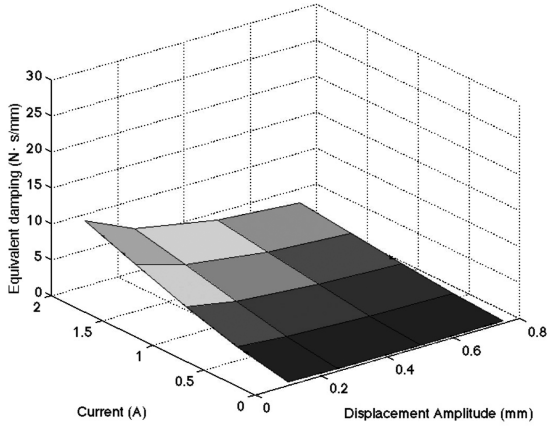

a) At 5Hz frequency

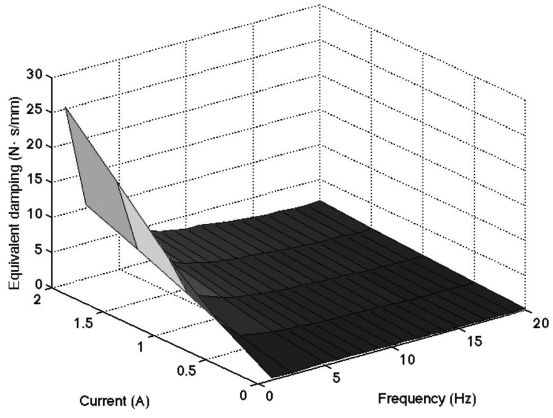

b) At ±0.25mm amplitude

Fig. 4 Measured equivalent viscous damping for the multiple fluid mode MR isolator.

$$E = \oint F\,\mathrm{d}x = \int_0^{2\pi/\omega} F\dot{x}\,\mathrm{d}t \tag{1}$$

and the equivalent viscous damping C_{eq} is given by

$$C_{\mathrm{eq}} = \frac{E}{\pi\omega X_0^2} \tag{2}$$

Here, X_0 is the amplitude of the displacement x.

Figure 4 shows the measured equivalent viscous damping for the multiple fluid mode MR isolator. The current input induces a large

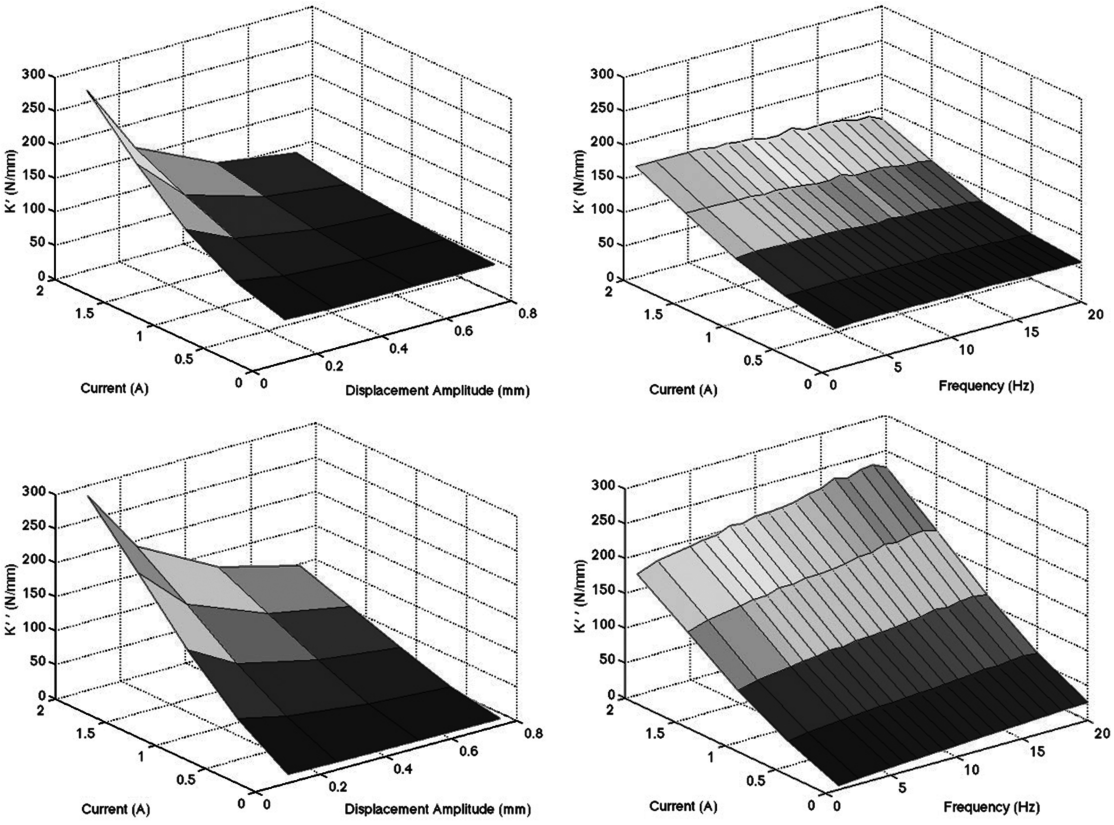

a) At 5Hz frequency **b) At ±0.25mm amplitude**

Fig. 5 Measured complex stiffness for the multiple fluid mode MR isolator.

increase in the equivalent viscous damping. However, as the displacement amplitude increases (see Fig. 4a), the equivalent viscous damping decreases. At zero current input, the equivalent viscous damping varies only slightly with the displacement amplitude. On the other hand, as the frequency increases (see Fig. 4b), the equivalent viscous damping for the MR isolator decreases. In addition, at zero current input, the equivalent viscous damping does not vary much with the frequency.

Alternatively, a linearization technique in the frequency domain, complex stiffness that represents force per unit displacement at a specified frequency, is used to measure the damping capacity of the multiple fluid mode MR isolator. In this approach, the complex stiffness K^* is characterized as an in-phase or storage stiffness K', which is a measure of the energy stored over a cycle and a loss stiffness K'', which is a measure of the energy dissipated over a period. This model can be represented as the Kelvin chain (a spring and viscous damper in parallel). The complex stiffness is expressed as [19–21]

$$K^* = K' + jK'' = K'(1 + \eta) \tag{3}$$

where η is the loss factor. When the multiple fluid mode MR isolator is subjected to a sinusoidal excitation, its displacement and velocity can be reconstructed as a Fourier series by

$$x(t) = X_c \cos(\omega t) + X_s \sin(\omega t) \tag{4}$$

$$\dot{x}(t) = -\omega X_c \sin(\omega t) + \omega X_s \cos(\omega t) \tag{5}$$

with

$$X_c = \frac{\omega}{\pi}\int_0^{2\pi/\omega} x(t)\cos(\omega t)\,\mathrm{d}t \quad \text{and} \quad X_s = \frac{\omega}{\pi}\int_0^{2\pi/\omega} x(t)\sin(\omega t)\,\mathrm{d}t \tag{6}$$

Similarly, the force of the MR isolator is also reconstructed using a

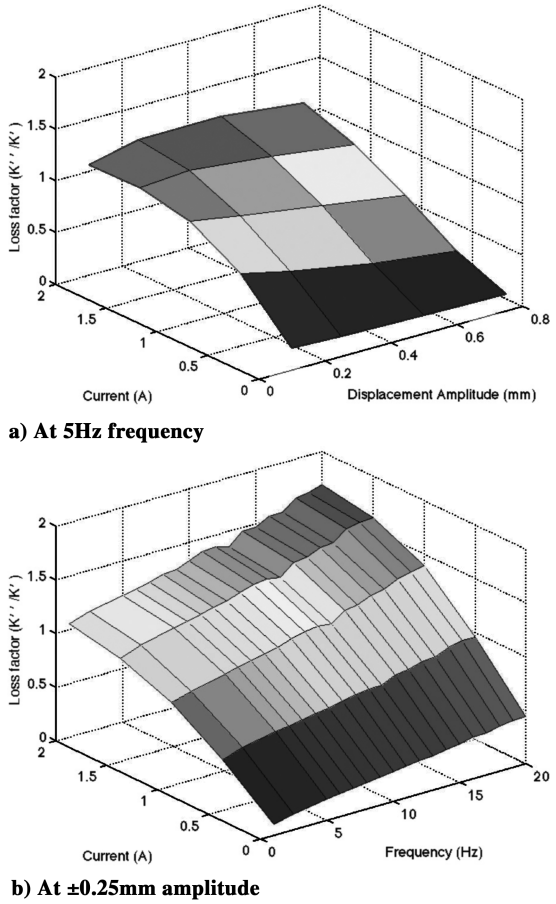

a) At 5Hz frequency

b) At ±0.25mm amplitude

Fig. 6 Measured loss factor for the multiple fluid mode MR isolator.

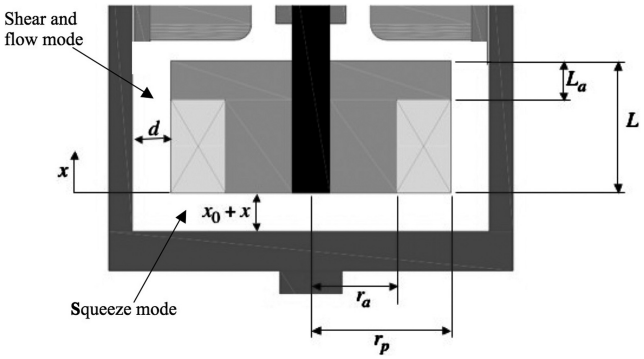

Fig. 7 Geometric parameters in the multiple fluid mode MR isolator.

Fourier series and is expressed in terms of the storage and loss stiffness as follows:

$$f(t) = F_c \cos(\omega t) + F_s \sin(\omega t) = K' x(t) + \frac{K''}{\omega}\dot{x}(t) \qquad (7)$$

where F_c and F_s are the cosine and sine Fourier coefficients of $f(t)$ at frequency ω.

Then, the storage and loss stiffnesses can be obtained from Eqs. (4–7) by

$$K' = \frac{F_c X_c + F_s X_s}{X_c^2 + X_s^2} \quad \text{and} \quad K'' = \frac{F_c X_s - F_s X_c}{X_c^2 + X_s^2} \qquad (8)$$

Figure 5 presents the measured complex stiffness for the multiple fluid mode MR isolator. As seen in Fig. 5, the storage and loss stiffness of the MR isolator is greatly increased by the current input. From Fig. 5a, it is observed that the storage and loss stiffness decreases with increasing the displacement amplitude. However, as the frequency increases, the storage stiffness decreases and the loss stiffness increases as shown in Fig. 5b.

Figure 6 presents the measured loss factor, $\eta(=K''/K')$ for the multiple fluid mode MR isolator. At the maximum current input, it is desired for the MR isolator to have a high loss factor over wide ranges of displacement amplitude as well as frequency. However, at zero current input, it is desired to have a low loss factor. It can be seen in Fig. 6 that, upon application of current, the loss factor is greatly increased over the entire range of amplitude as well as frequency.

Bingham-Plastic Isolator Model

The multiple fluid mode MR damper has two regions of fluid flow resulting from axial motion of the bobbin as shown in Fig. 7. In the gap between the bottom of the bobbin and the bottom of the outer cylinder, motion of the bobbin compresses the fluid and flow in the radial direction results. This region behaves as a squeeze-mode damper. In the annulus between the side of the bobbin and the walls of the outer cylinder, fluid flow is induced by a combination of 1) a pressure differential developed through the annulus due to motion of the bobbin and 2) a direct shearing of the fluid as the bobbin moves relative to the outer cylinder. This region behaves as a combination shear- and flow-mode damper. Therefore, the total force of the MR isolator can be theoretically obtained by a superposition of the force developed by each operating mode of the fluid as well as the force provided by the elastomer.

The elastomer is modeled as a spring-damper; its force is given by

$$F_{el} = K_{el} x + C_{el} \dot{x} \qquad (9)$$

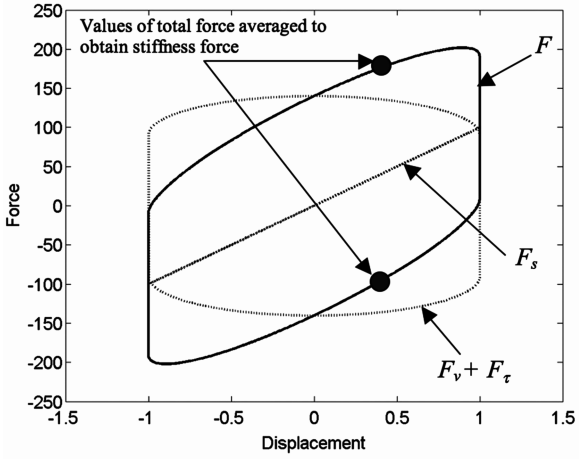

a) Force-displacement plot

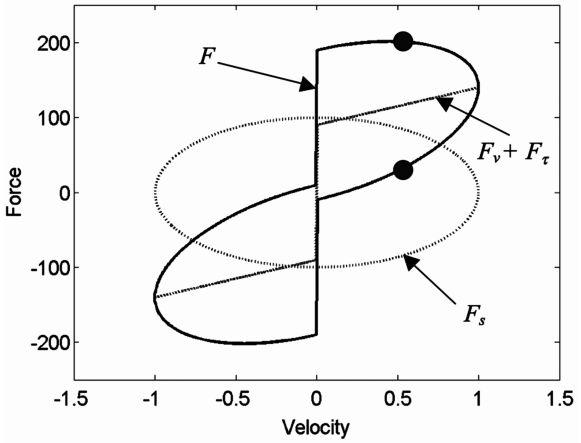

b) Force-velocity plot

Fig. 8 Typical force-displacement and force-velocity plots of an MR isolator using Eq. (16).

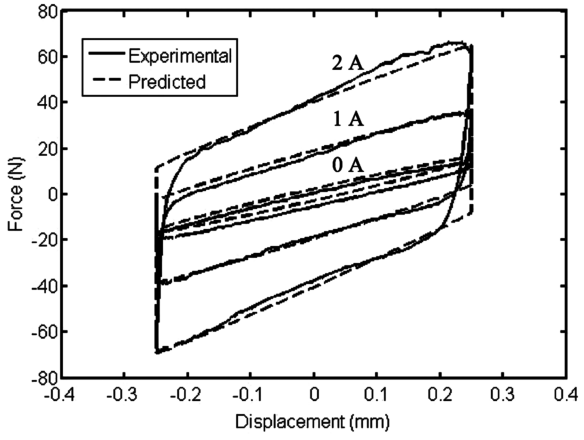

a) Force vs displacement

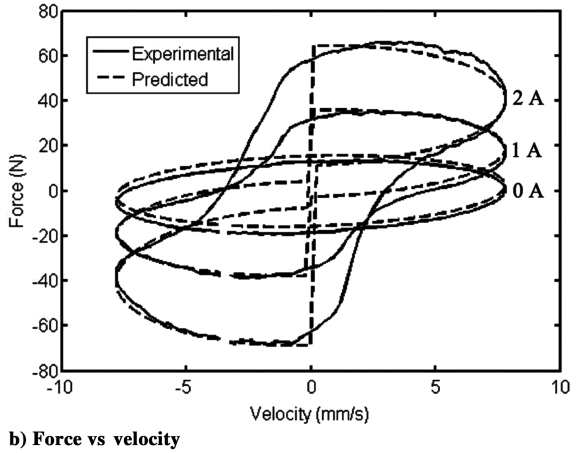

b) Force vs velocity

Fig. 9 Comparison of the measured and predicted responses of the multiple fluid mode MR isolator using the Bingham-plastic isolator model (5 Hz and ±0.25 mm).

Here, K_{el} and C_{el} are the stiffness and damping of the elastomer, respectively.

The force of the MR isolator due to the shear flow is given as [3,4]

$$F_{shear} = \frac{\mu bL}{d}\dot{x} + bL_a\tau_{y,sh}\,\mathrm{sgn}(\dot{x}) \tag{10}$$

Here, d is the gap between the side of the bobbin and the walls of the outer cylinder, b is the width (that is a perimeter of the bobbin and equal to $2\pi r_p$), r_p is the radius of the bobbin, L is the bobbin length, and L_a is the active length to activate the MR fluid in shear and flow modes. The fluid viscosity is μ, and $\tau_{y,sh}$ is the yield stress of the MR fluid in shear mode.

The force of the MR isolator due to the flow mode is given by [12,13]

$$F_{flow} = \frac{12A_P^2\mu L}{bd^3}\dot{x} + \frac{2A_PL_a\tau_{y,fl}}{d}\,\mathrm{sgn}(\dot{x}) \tag{11}$$

Here, A_p is the effective piston area and $\tau_{y,fl}$ is the yield stress of the MR fluid in flow mode.

The force due to the squeeze flow is given as [17,18]

$$F_{squeeze} = \frac{3\pi\mu r_p^4}{2(x_0+x)^3}\dot{x} + \frac{4\pi\tau_{y,sq}r_a^3}{3(x_0+x)}\,\mathrm{sgn}(\dot{x}) \tag{12}$$

Here, r_a is the active radius to activate the MR fluid in squeeze mode, x_0 is the initial gap between the bottom of the bobbin and the bottom of the outer cylinder, and $\tau_{y,sq}$ is the yield stress of the MR fluid in squeeze mode.

Then, the total force of the multiple fluid mode MR isolator is obtained as follows:

$$\begin{aligned} F_d &= F_{el} + F_{shear} + F_{flow} + F_{squeeze} \\ &= K_{el}x + (C_{el}+C)\dot{x} + F_y\,\mathrm{sgn}(\dot{x}) \end{aligned} \tag{13}$$

where the total fluid damping due to each fluid mode C is given by

$$C = \frac{\mu bL}{d} + \frac{12A_P^2\mu L}{bd^3} + \frac{3\pi\mu r_p^4}{2(x_0+x)^3} \tag{14}$$

and the total yield force due to each fluid mode F_y is given by

$$F_y = bL_a\tau_{y,sh} + \frac{2A_PL_a\tau_{y,fl}}{d} + \frac{4\pi\tau_{y,sq}r_a^3}{3(x_0+x)} \tag{15}$$

Note that, as mentioned before, shear- and flow-mode damping occurs along the side of the bobbin, whereas squeeze-mode damping occurs in the area below the bobbin. As these damping modes occur in separate areas of the MR device, the strength of the magnetic field could vary between these areas, causing the yield stress of the fluid for the shear and flow modes ($\tau_{y,sh}$, $\tau_{y,fl}$) to be different than that of the squeeze mode $\tau_{y,sq}$. For simplicity, it was assumed that the magnetic field was equal in the two areas and that the yield stress of the fluid in the squeeze-mode effect would be the same as the yield stress of the fluid in the shear- and flow-mode effect, $\tau_{y,sh} = \tau_{y,fl} = \tau_{y,sq} = \tau_y$.

To implement the Bingham-plastic (BP) isolator model, knowledge of the fluid properties μ and τ_y, as well as the damping and stiffness properties of the elastomer C_{el} and K_{el}, is needed. Because the equivalent viscous damping at zero field input is almost constant over wide ranges of displacements and frequencies, the fluid viscosity and the damping of the elastomer are chosen to be constants by $\mu = 0.09$ Pa · s and $C_{el} = 0.3$ N/mm. However, K_{el} and τ_y are strongly dependent on the frequency, the displacement amplitude, and the current input. In this study, the averaging method [22] using the force-displacement plot and the force-velocity plot is used to identify the model parameters of K_{el} and τ_y.

To explain the averaging identification method, consider the simple model of an MR isolator under a sinusoidal excitation

$$F = F_s + F_v + F_\tau \tag{16}$$

where F is the total damper force, $F_s = K_sx$ is the stiffness force, $F_v = C_v\dot{x}$ is the viscous force, $F_\tau = F_{\tau_0}\,\mathrm{sgn}(\dot{x})$ is the yield force, K_s is the stiffness, C_v is the viscous damping, and F_{τ_0} is the yield force magnitude. Figure 8 shows typical force-displacement and force-velocity plots of an MR isolator using Eq. (16). In the force-displacement plot as shown in Fig. 8a, the stiffness force F_s increases linearly with the displacement, but the viscous and yield forces $F_v + F_\tau$ are symmetric about the zero force axis and show elliptical shape. If averaging the force F for a given value of displacement in the force-displacement plot (refer to Fig. 8a), the viscous and yield forces $F_v + F_\tau$ will be cancelled, leaving only the stiffness force in the force-displacement plot. The slope of the stiffness force around the zero x axis in the force-displacement plot yields the stiffness of the elastomer K_{el}. On the other hand, in a similar way, the average of the force F, for a given value of velocity in the force-velocity plot (refer to Fig. 8b), extracts the viscous and yield force out of the total force because the stiffness force F_s is cancelled out. From the extracted viscous and yield force $F_v + F_\tau$, the yield force magnitude is obtained by

$$F_{\tau_0} = |F_v + F_\tau - C_v\dot{x}| \tag{17}$$

Setting the average yield force magnitude F_{τ_0} at the maximum and minimum velocities equal to the theoretical yield force in Eq. (15) gives the identified yield stress as follows:

$$\tau_y = \frac{F_{\tau_0}}{bL_a + (2A_PL_a/d) + (4\pi r_a^3/3x_0)} \tag{18}$$

Figure 9 presents the comparison of the measured and predicted responses of the multiple fluid mode MR damper using the BP isolator model. The BP isolator model does not describe the

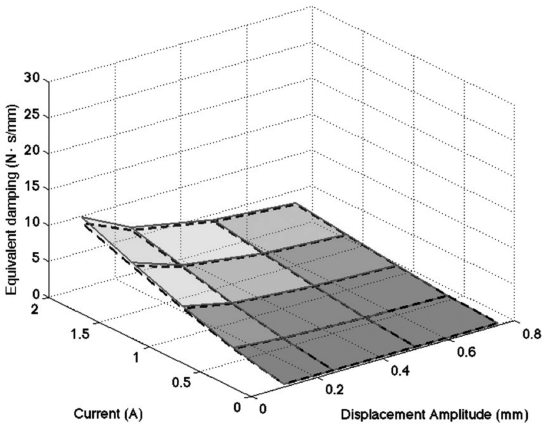

a) At 5Hz frequency

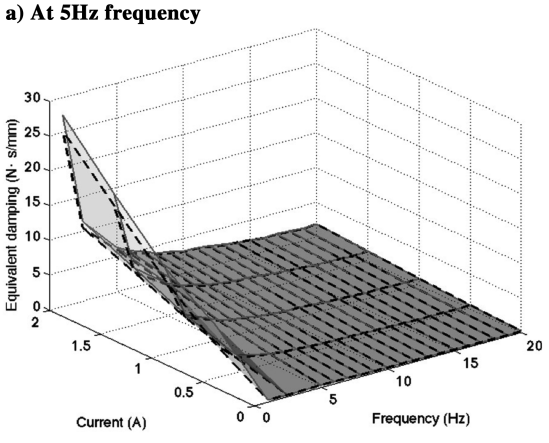

b) At ±0.25mm amplitude

Fig. 10 Comparison of the measured and predicted equivalent viscous damping of the multiple fluid mode MR isolator using the Bingham-plastic isolator model (5 Hz and ±0.25 mm).

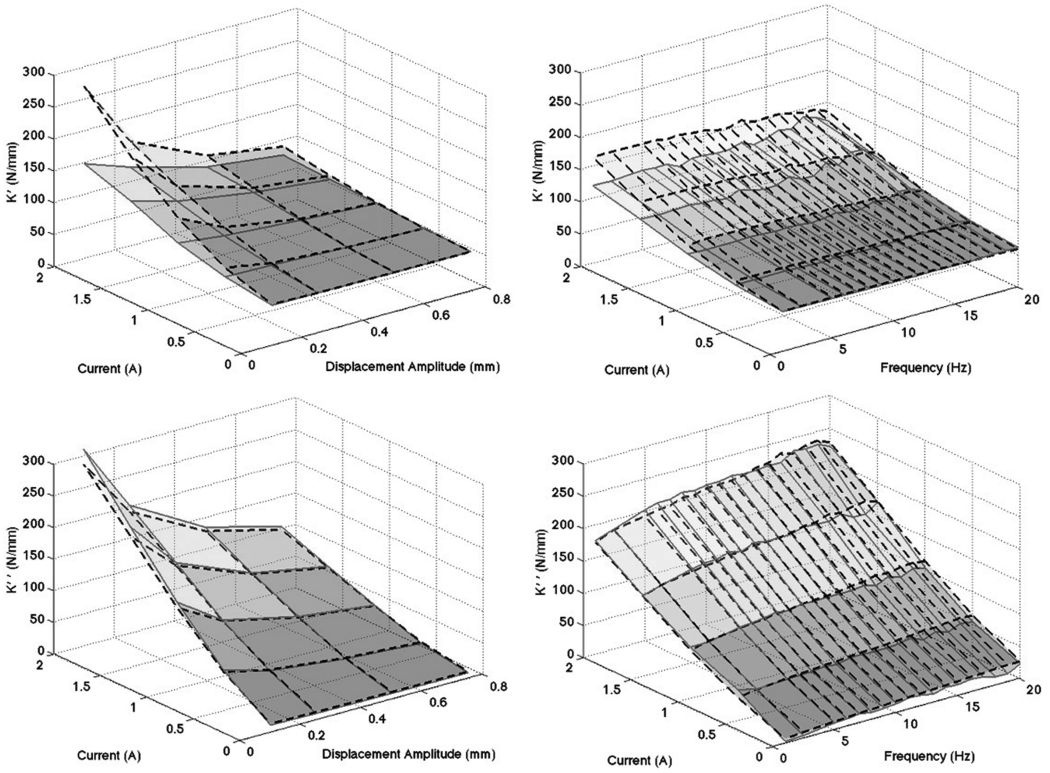

a) At 5Hz frequency **b) At ±0.25mm amplitude**

Fig. 11 Comparison of the measured and predicted complex stiffness of the multiple fluid mode MR isolator using the Bingham-plastic isolator model.

hysteresis loop in the force-velocity plot well, but can favorably capture average behavior of the MR isolator.

Figure 10 presents the comparison of the measured and predicted equivalent viscous damping responses of the multiple fluid mode MR damper using the BP isolator model. In this case, the dashed line stands for the measured data and the solid line represents the predicted data. The BP isolator model can capture the experimental equivalent viscous damping behaviors well over the entire range of amplitudes as well as frequencies.

Figure 11 presents the comparison of the experimental and predicted complex stiffness of the multiple fluid mode MR isolator using the BP isolator model. In this case, the dashed line stands for the measured data and the solid line represents the predicted data. The predicted loss stiffness K'' is in good agreement with the experimental results. However, the predicted storage stiffness K' is lower than the experimental results. The difference between the experimental and predicted storage stiffness results from the fact the BP isolator model does not consider the hysteresis loop in the force-velocity data. The hysteresis in the force-velocity data causes the storage stiffness to be underpredicted relative to the measured storage stiffness.

Figure 12 presents the comparison of the experimental and predicted loss factor of the multiple fluid mode MR isolator using the BP isolator model. In this case, the dashed line stands for the measured data and the solid line represents the predicted data. At higher current input and lower displacement amplitude, the discrepancy between the measured and predicted loss factor becomes larger. Because of the underprediction of the predicted storage stiffness, the predicted loss factor becomes much larger than the measured one.

Figure 13 presents the comparison of the reconstructed forces between the experimental and predicted complex stiffness using the BP isolator model. In this case, the reconstructed forces were obtained from Eq. (7) using the identified complex stiffness. The slope of the reconstructed force in the force-displacement plot implies the storage stiffness K' of the MR isolator. Because the experimental storage stiffness K' is greater than the predicted storage stiffness K'_{model} in Fig. 13b, the slope of the reconstructed force using

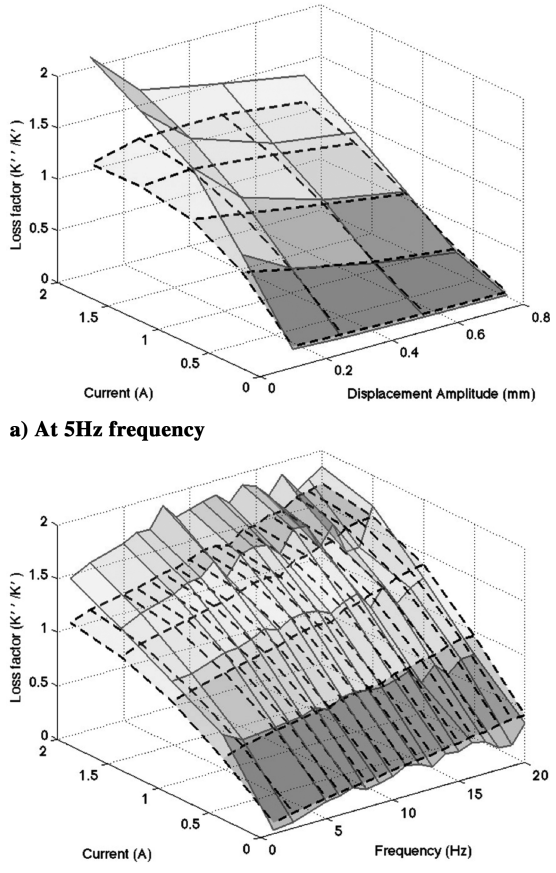

a) At 5Hz frequency

b) At ±0.25mm amplitude

Fig. 12 Comparison of the measured and predicted loss factor of the multiple fluid mode MR isolator using the Bingham-plastic isolator model (5 Hz and ±0.25 mm).

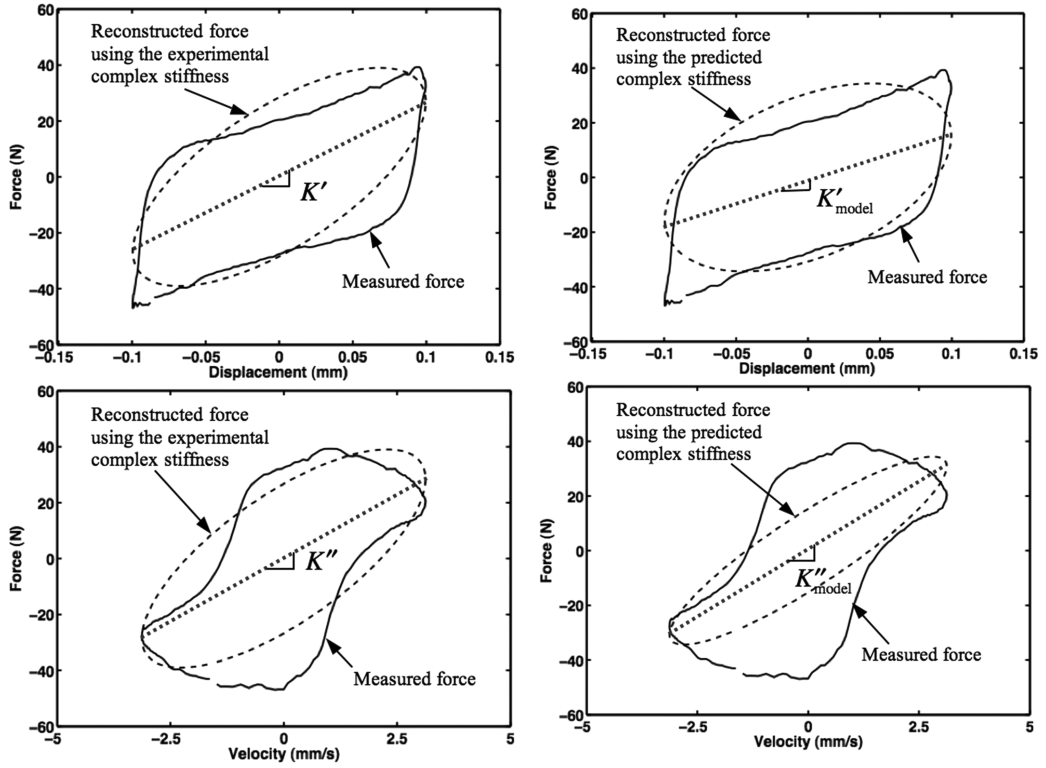

a) Experimental complex stiffness **b) Predicted complex stiffness**

Fig. 13 Comparison of the reconstructed forces using the experimental and predicted complex stiffness using the Bingham-plastic isolator model (5 Hz and ±0.1 mm).

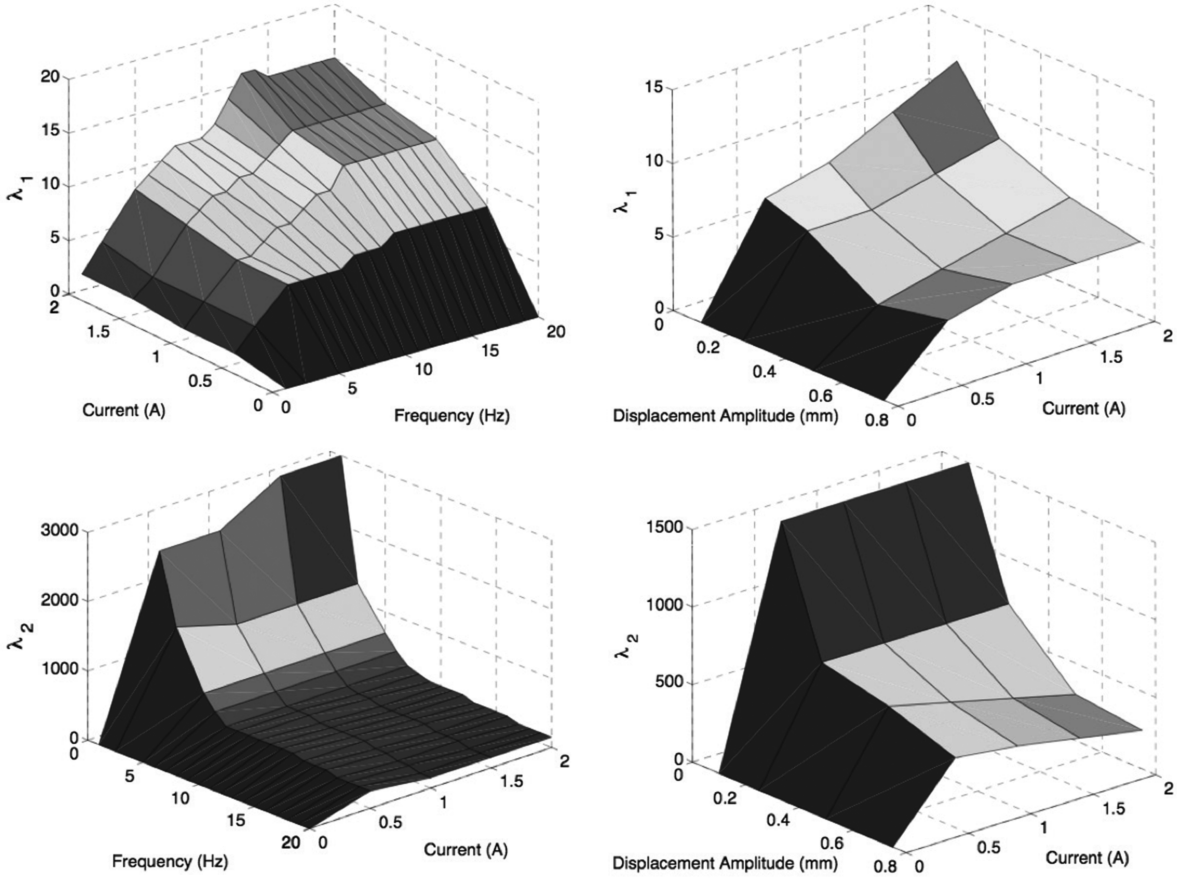

a) At ±0.25mm amplitude **b) At 5Hz frequency**

Fig. 14 Identified parameters λ_1 and λ_2 of the nonlinear hysteretic Bingham-plastic isolator model.

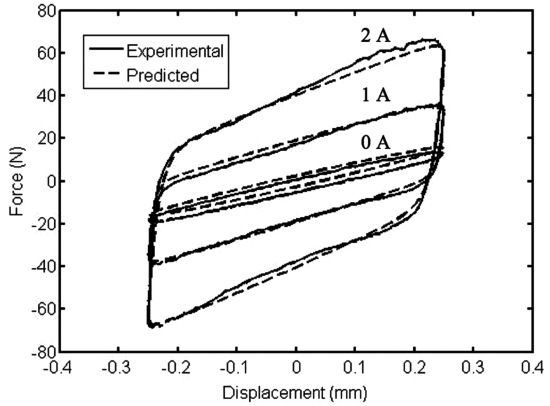

a) Force vs displacement

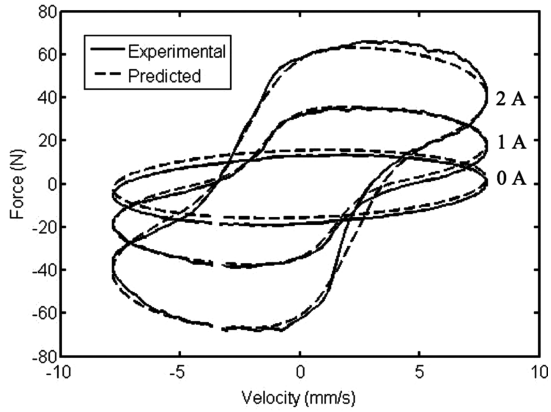

b) Force vs velocity

Fig. 15 Comparison of the measured and predicted responses of the multiple fluid mode MR isolator using the nonlinear hysteretic Bingham-plastic isolator model (5 Hz and ±0.25 mm).

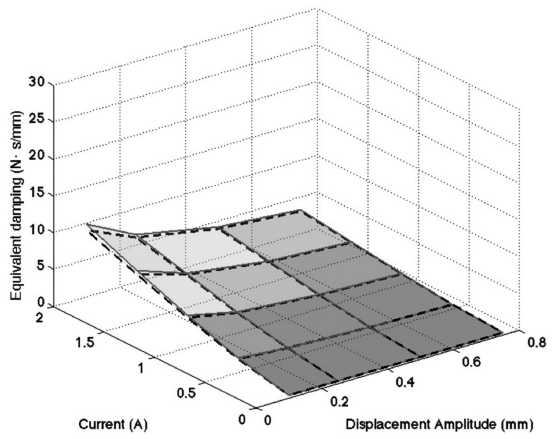

a) At 5Hz frequency

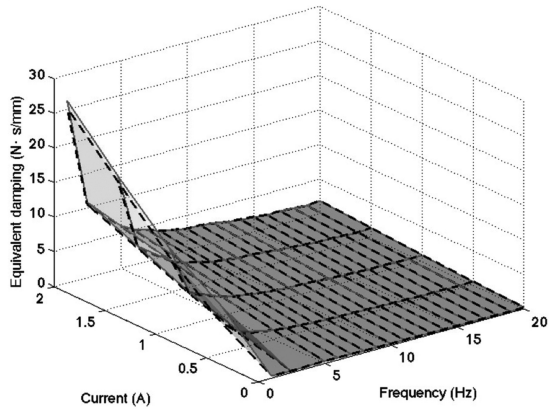

b) At ±0.25mm amplitude

Fig. 16 Comparison of the measured and predicted equivalent viscous damping of the multiple fluid mode MR isolator using the nonlinear hysteretic Bingham-plastic isolator model (5 Hz and ±0.25 mm).

the experimental complex stiffness is steeper than that using the predicted stiffness. In addition, a larger storage stiffness causes the enclosed area of the reconstructed force in the force-velocity plot to increase so as to capture the hysteresis loop in the force-velocity plot. However, because the predicted storage stiffness was obtained based on the BP isolator model that does not consider the hysteresis loop in the force-velocity plot, it becomes smaller than the experimental complex stiffness. On the other hand, the slope of the reconstructed force in the force-velocity plot represents the loss stiffness K'' of the MR isolator. As seen in Fig. 13, the slope in the force-velocity plot using the experimental complex stiffness is similar to that using the predicted complex stiffness because the predicted and measured loss stiffnesses are nearly equal (see Fig. 11). As a result, the loss factor $\eta = (K''/K')$ of the BP isolator model will be overpredicted compared to that of the measured loss factor because the predicted storage stiffness is smaller than the measured storage stiffness.

Nonlinear Hysteretic Bingham-Plastic Isolator Model

The BP isolator model mentioned in the preceding section captures overall damper behavior in the force-displacement and force-velocity plots. In addition, it gives a good agreement with the experimental loss stiffness plot, but underpredicts the storage stiffness because the yield force of the BP isolator model has the discontinuous behavior at zero velocity. To improve the BP isolator model, a nonlinear hysteretic model will be introduced. The nonlinear hysteretic Bingham-plastic (NHBP) isolator model replaces the zero speed force step discontinuity present in the BP isolator model with more gradual transition through the low-speed regime. This resulted in a more accurate portrayal of the hysteresis characteristics of the MR isolator.

The force of the MR isolator in the NHBP model is given by [23]

$$F_d = K_{\text{el}}x + (C_{\text{el}} + C)\dot{x} + F_y \tanh[\lambda_2(\dot{x} + \lambda_1 x)] \qquad (19)$$

where λ_1 and λ_2 are characteristic parameters used to capture the hysteresis loop in the force-velocity plot. The parameter λ_1 accounts for the width of the hysteresis loop and λ_2 accounts for the slope of the hysteresis loop. To fully establish the structure of the hysteresis isolator model, these parameters were found using a curve-fitting method so as to match the experimental results. Figure 14 shows the identified parameters λ_1 and λ_2 of the NHBP isolator model. The parameter λ_1 is found to be strongly dependent upon excitation frequency, displacement amplitude, and the applied current. The parameter λ_2 has a strong dependence upon excitation frequency and displacement amplitude and a weaker correlation with the applied current.

Figure 15 presents the comparison of the measured and predicted responses of the multiple fluid mode MR isolator based on the NHBP isolator model. The hysteresis isolator model correlates well with experimental data. The ability of the hysteresis isolator model to capture the hysteresis behavior is evident, especially at low speed when the Bingham isolator model failed to accurately predict isolator force.

Figure 16 presents the comparison of the measured and predicted equivalent viscous damping of the multiple fluid mode MR isolator using the NHBP isolator model. In this case, the dashed line stands for the measured data and the solid line represents the predicted data. As expected from Fig. 15, the predicted damping of the MR isolator correlates well with the experimental results.

Figure 17 presents the comparison between the measured and predicted complex stiffness of the multiple fluid mode MR isolator under the NHBP isolator model. In this case, the dashed line stands for the measured data and the solid line represents the predicted data. The NHBP isolator model captures the behavior of the experimental storage stiffness very well over most of the displacement amplitudes and frequency ranges. The inclusion of a hysteresis loop, which

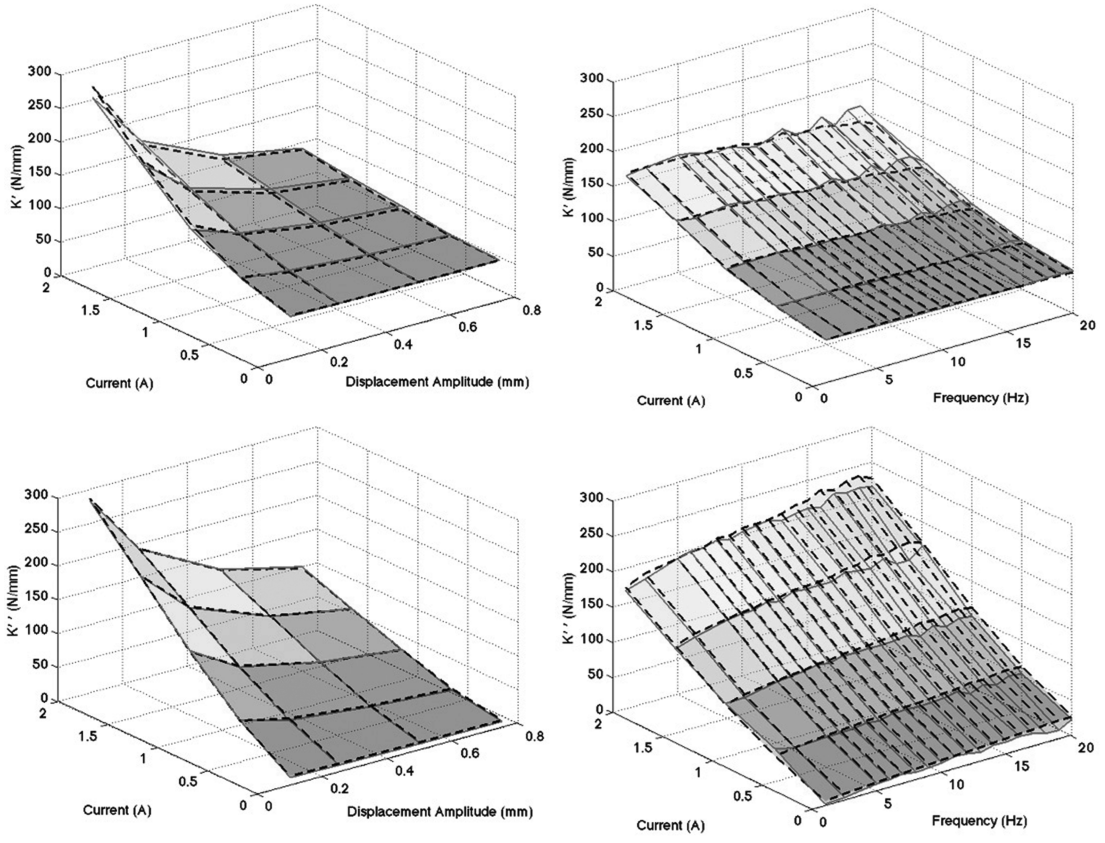

a) At 5Hz frequency **b) At ±0.25mm amplitude**

Fig. 17 Comparison of the measured and predicted complex stiffness of the multiple fluid mode MR isolator using the nonlinear hysteretic Bingham-plastic isolator model (5 Hz and ±0.25 mm).

resulted from accurately capturing the transition behavior of the MR yield force, produced a model more capable of predicting the complex stiffness of the MR isolator.

Figure 18 presents the comparison of the experimental and predicted loss factor of the multiple fluid mode MR isolator using the NHBP isolator model. In this case, the dashed line stands for the measured data and the solid line represents the predicted data. As expected, the predicted loss factor is well matched with the measured one.

Model Comparison

To compare the two isolator models used to predict the MR isolator behavior quantitatively, the complex correlation coefficient (CCF) was used [24,25]. The CCF is a numerical method, which compares the perimeters of two-dimensional objects to assess their similarity. The CCF is a quantitative measure of the shape and phase of model fit. A CCF of one indicates a perfect model fit. In this case, two different CCFs were used for the comparison of the measured and predicted responses over the force-displacement cycles and the force-velocity cycles, respectively. In the CCF Φ_d, for the force-displacement cycles, the boundary functions are given by

$$h_d(t) = x(t) + jF_d(t) \qquad \hat{h}_d(t) = x(t) + j\hat{F}_d(t) \tag{20}$$

Here, F_d is the measured force of the multiple fluid mode MR isolator and $\hat{F}_d$ are the predicted isolator force obtained from each isolator model. Then, the CCF Φ_d for the force-displacement cycles is given by

$$\Phi_d = \frac{\int h_d(t)\hat{h}_d^*(t)\,\mathrm{d}t}{\{[\int h_d(t)h_d^*(t)\,\mathrm{d}t][\int \hat{h}_d(t)\hat{h}_d^*(t)\,\mathrm{d}t]\}^{1/2}} \tag{21}$$

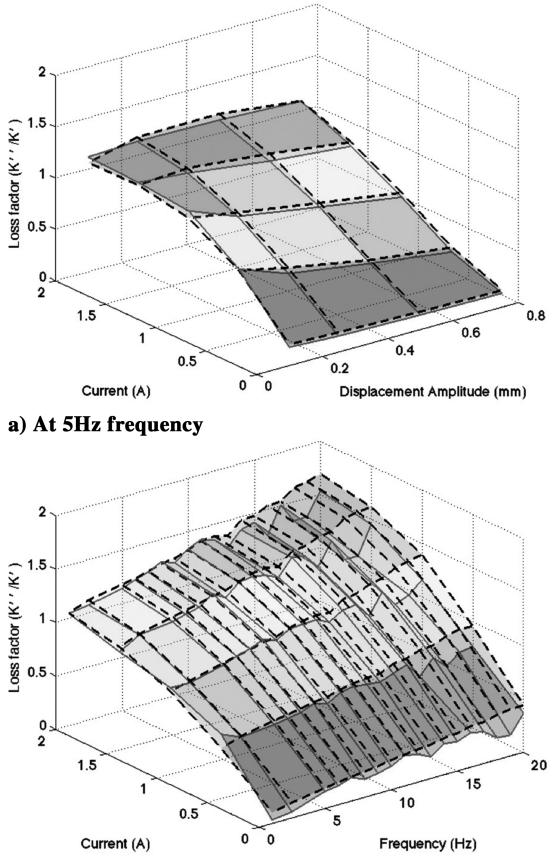

a) At 5Hz frequency

b) At ±0.25mm amplitude

Fig. 18 Comparison of the measured and predicted loss factor of the multiple fluid mode MR isolator using the nonlinear hysteretic Bingham-plastic isolator model (5 Hz and ±0.25 mm).

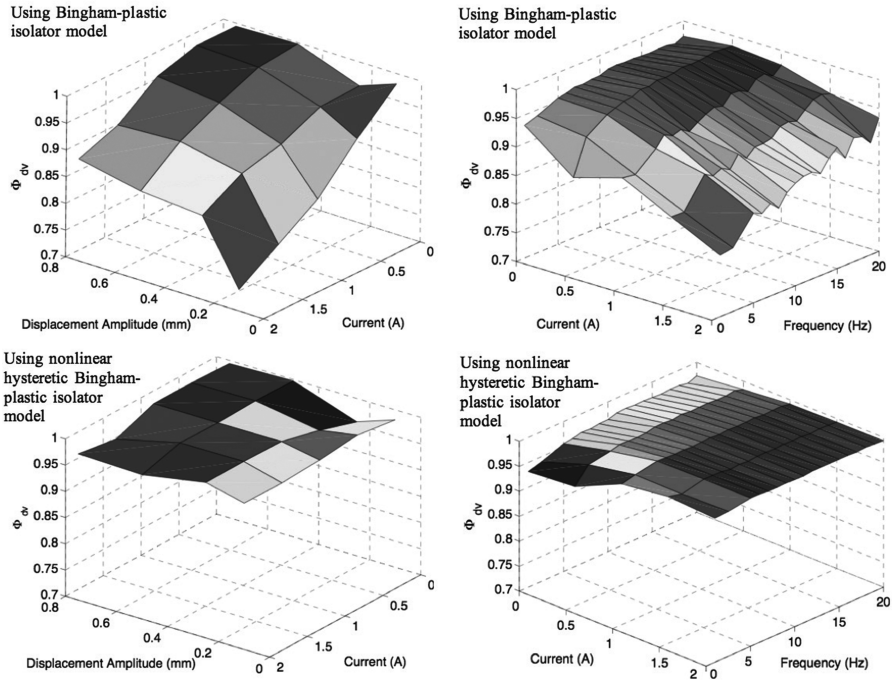

a) At 5Hz frequency **b) At ±0.25mm amplitude**

Fig. 19 Comparison of the complex correlation factor $\Phi_{dv}(=\Phi_d \cdot \Phi_v)$ between using the Bingham-plastic and nonlinear hysteretic Bingham-plastic isolator models.

where $h_d^*(t)$ and $\hat{h}_d^*(t)$ are the complex conjugates of $h_d(t)$ and $\hat{h}_d(t)$. In a similar way, the CCF Φ_v for the force-velocity cycles is defined. However, the boundary functions for Φ_v are as follows:

$$h_v(t) = \dot{x}(t) + jF_d(t) \qquad \hat{h}_v(t) = \dot{x}(t) + j\hat{F}_d(t) \tag{22}$$

Figure 19 presents the comparison of the CCF $\Phi_{dv}(=\Phi_d \cdot \Phi_v)$ of the multiple fluid mode MR isolator between using the BP and NHBP isolator models. As seen in Fig. 19a, the lowest CCF Φ_{dv} of the BP isolator model for the 5 Hz excitation frequency case is 0.74. However, for the same case, the lowest CCF Φ_{dv} of the NHBP isolator model is 0.96. This implies that the NHBP isolator model improves the model prediction ability up to 30% over the measured range of the displacement amplitude and current input. On the other hand, the lowest CCFs Φ_{dv} of the BP and NHBP isolator models for ± 0.25 mm displacement amplitude shown in Fig. 19b are 0.81 and 0.93, respectively. This implies that the NHBP isolator model predictions are improved by 15% over the range of excitation frequency and current input.

Conclusions

In this study, the experimental and theoretical analyses of the multiple fluid mode MR isolator were conducted. For doing so, a multiple fluid mode MR isolator using the shear, flow, and squeeze modes was configured and fabricated. The damper characteristics of the MR isolator were experimentally evaluated using metrics of equivalent viscous damping and complex stiffness. A BP isolator model was constructed and its important model parameters such as the stiffness of the elastomer and the yield stress were identified using the average method derived from sinusoidal force-displacement and force-velocity data. Comparison of the experimental and theoretical results using the BP isolator model was conducted. Predicted equivalent viscous damping is in good agreement with the experimental results. The predicted loss stiffness is also in good agreement with the experimental results. However, the predicted storage stiffness is smaller than the experimental results because the BP isolator model does not consider the hysteresis loop in the force-velocity plot. As a result, the NHBP isolator model, which replaced the zero speed force step discontinuity present in the BP isolator model with more gradual transition through the low-speed regime, was constructed. To construct the NHBP isolator model, its model parameters λ_1 and λ_2 are identified using a curve-fitting method. Comparison of the two different isolator models over the damping capability plots, such as the force displacement, force velocity, equivalent viscous damping, and the complex stiffness, was conducted. As a result, it was observed that the NHBP model, which incorporates a displacement-velocity dependent hypertangent function to capture the hysteresis loop, can predict the storage stiffness of the MR isolator well. For a quantitative comparison of the model prediction ability between two isolator models, the complex correlation coefficient was used. For the BP isolator model, the lowest CCF, Φ_{dv}, over all of the tested conditions was 0.74. However, the lowest CCF Φ_{dv} for the NHBP model over all of the tested conditions was 0.93. A CCF of one implies the perfect match between the experimental and predicted results, so that the NHBP isolator model improved the model prediction ability by 26% overall.

References

[1] Lee-Glauser, G. J., Ahmadi, G., and Layton, J. B., "Satellite Active and Passive Vibration Control During Liftoff," *Journal of Spacecraft and Rockets*, Vol. 33, No. 3, 1996, pp. 428–432.

[2] Cobb, R. G., Sullivan, J. M., Das, A., Davis, L. P., Hyde, T. T., Davis, T., Rahman, Z. H., and Spanos, J. T., "Vibration Isolation and Suppression System for Precision Payloads in Space," *Smart Materials and Structures*, Vol. 8, No. 6, 1999, pp. 798–812. doi:10.1088/0964-1726/8/6/309

[3] Choi, S. B., and Choi, Y. T., "Sliding Mode Control of Shear-Mode Type ER Engine Mount," *KSME International Journal*, Vol. 13, No. 1, 1999, pp. 26–33.

[4] Choi, S. B., Choi, Y. T., Cheong, C. C., and Jeon, Y. S., "Performance Evaluation of a Mixed Mode ER Engine Mount via Hardware-in-the-Loop Simulation," *Journal of Intelligent Material Systems and Structures*, Vol. 10, No. 8, 1999, pp. 671–677. doi:10.1106/KR86-XWN0-JR8J-5WRX

[5] Lou, Z., Ervin, R. D., Filisko, F. E., and Winkler, C. B., "*Electrorheologically Controlled Semi-Active Landing Gear*," Society of Automotive Engineers TP Series 931403, 1993.

[6] Lou, Z., Ervin, R. D., and Filisko, F. E., "Preliminary Parametric Study of Electrorheological Dampers," *Journal of Fluids Engineering*, Vol. 116, No. 3, 1994, pp. 570–576.

[7] Wereley, N. M., and Pang, L., "Nondimensional Analysis of Semi-Active Electrorheological and Magnetorheological Dampers Using

Approximate Parallel Plate Models," *Smart Materials and Structures*, Vol. 7, No. 5, 1998, pp. 732–743.
doi:10.1088/0964-1726/7/5/015

[8] Gavin, H. P., Hanson, R. D., and Filisko, F. E., "Electrorheological Dampers, Part 1: Analysis and Design," *Journal of Applied Mechanics*, Vol. 63, No. 3, 1996, pp. 669–675.

[9] Gordaninejad, F., Ray, A., and Wang, H., "Control of Forced Vibration Using Multi-Electrode Electrode-Rheological Fluid Dampers," *Journal of Vibration and Acoustics*, Vol. 119, No. 4, 1997, pp. 527–531.

[10] Sims, N. D., Peel, D. J., Stanway, R., Johnson, A. R., and Bullough, W. A., "Electrorheological Long-Stroke Damper: A New Modelling Technique with Experimental Validation," *Journal of Sound and Vibration*, Vol. 229, No. 2, 2000, pp. 207–227.
doi:10.1006/jsvi.1999.2487

[11] Lindler, J. E., Choi, Y. T., and Wereley, N. M., "Double Adjustable Shock Absorbers Utilizing Electrorheological and Magnetorheological Fluids," *International Journal of Vehicle Design: The Journal of the International Association for Vehicle Design*, Vol. 33, Nos. 1–3, 2003, pp. 189–206.
doi:10.1504/IJVD.2003.003571

[12] Choi, S. B., Choi, Y. T., Chang, E. G., Han, S. J., and Kim, C. S., "Control Characteristics of a Continuously Variable ER Damper," *Mechatronics*, Vol. 8, No. 2, 1998, pp. 143–161.
doi:10.1016/S0957-4158(97)00019-6

[13] Choi, Y. T., and Wereley, N. M., "Vibration Control of a Landing Gear System Featuring Electrorheological/Magnetorheological Fluids," *Journal of Aircraft*, Vol. 40, No. 3, 2003, pp. 432–439.

[14] Stanway, R., Sproston, J. L., and El-Wahed, A. K., "Applications of Electro-Rheological Fluids in Vibration Control: A Survey," *Smart Materials and Structures*, Vol. 5, No. 4, 1996, pp. 464–482.
doi:10.1088/0964-1726/5/4/011

[15] Stanway, R., Sproston, J. L., Prendergast, M. J., Case, J. R., and Wilne, C. E., "ER Fluids in the Squeeze-flow Mode: An Application to Vibration Isolation," *Journal of Electrostatics*, Vol. 28, No. 1, May 1992, pp. 89–94.
doi:10.1016/0304-3886(92)90029-S

[16] Williams, S., Rigby, S. G., Sproston, J. L., and Stanway, R., "Electrorheological Fluids Applied to an Automotive Engine Mount," *Journal of Non-Newtonian Fluid Mechanics*, Vol. 47, June 1993, pp. 221–238.
doi:10.1016/0377-0257(93)80052-D

[17] Jolly, M. R., and Carlson, J. D., "Controllable Squeeze Film Damping Using Magnetorheological Fluid," *5th International Conference on New Actuators*, Axon Technologies, Bremen, Germany, 1996, pp. 333–336.

[18] Hong, S. R., Choi, S. B., Jung, W. J., and Jeong, W. B., "Vibration Isolation of Structural Systems Using Squeeze Mode ER Mounts," *Journal of Intelligent Material Systems and Structures*, Vol. 13, Nos. 7–8, 2002, pp. 421–424.

[19] Tse, F. S., Morse, I. E., and Hinkle, R. T., *Mechanical Vibrations: Theory and Applications*, 2nd ed., Allyn and Bacon, Boston, 1978.

[20] Hu, W., Wereley, N. M., Chemounis, L., and Chen, P. C., "Semi-Active Linear Stroke Magnetorheological Fluid-Elastic Helicopter Lag Damper," *Journal of Guidance, Control, and Dynamics*, Vol. 30, No. 2, 2007, pp. 565–575.
doi:10.2514/1.24033.

[21] Goege, D., "Fast Identification and Characterization of Nonlinearities in Experimental Modal Analysis of Large Aircraft," *Journal of Aircraft*, Vol. 44, No. 2, 2007, pp. 399–409.
doi:10.2514/1.20847

[22] Hu, W., and Wereley, N. M., "Characterization and Modeling of Nonlinear Elastomeric Dampers Under Sinusoidal Loading," *44th AIAA/ASME/ASCE/AHS Structures, Structural Dynamics, and Material Conference*, AIAA 2003-1819, 2003.

[23] Choi, Y. T., Wereley, N. M., and Jeon, Y. S., "Semi-Active Vibration Isolation Using Magnetorheological Isolators," *Journal of Aircraft*, Vol. 42, No. 5, 2005, pp. 1244–1251.

[24] Cleveland, D., O'Brien, L. J., and Wereley, N. M., "Automated Aid for Isolating Defects in the Heat Exchanger Tubing of Nuclear Steam Generators," *Instrument Society of America Transactions*, Vol. 25, No. 3, 1986, pp. 61–71.

[25] Snyder, R., Kamath, G. M., and Wereley, N. M., "Characterization and Analysis of Magnetorheological Damper Behavior Under Sinusoidal Loading," *AIAA Journal*, Vol. 39, No. 7, 2001, pp. 1240–1253.